PAPER

Facile one-step hydrothermal synthesis of single-crystalline $SnNb_2O_6$ nanosheets with greatly extended visible-light response for enhanced photocatalytic performance and mechanism insight

To cite this article: Qianqian Liu *et al* 2021 *Nanotechnology* **32** 065705

IOP Publishing Nanotechnology
Nanotechnology 32 (2021) 065705 (13pp) https://doi.org/10.1088/1361-6528/abc3e3

Facile one-step hydrothermal synthesis of single-crystalline $SnNb_2O_6$ nanosheets with greatly extended visible-light response for enhanced photocatalytic performance and mechanism insight

Qianqian Liu[1,*], Quan Zhang[2], Bo Liu[1] and Wei-Lin Dai[2,*]

[1] Research Center for Nanophotonic and Nanoelectronic Materials, School of Chemistry, Biology and Materials Engineering, Suzhou University of Science and Technology, Suzhou 215009, Jiangsu Province, People's Republic of China
[2] Department of Chemistry and Shanghai Key Laboratory of Molecular Catalysis and Innovative Materials, Fudan University, Shanghai 200433, People's Republic of China

E-mail: liuqianqian@usts.edu.cn and wldai@fudan.edu.cn

Received 1 September 2020, revised 10 October 2020
Accepted for publication 22 October 2020
Published 19 November 2020

Abstract

The conventional preparation of $SnNb_2O_6$ invariably involves complex and laborious steps, which unavoidably introduces defect into the host lattice and also increases the reaction period and costs, resulting in undesired recombination of photo-generated electron–hole pairs. For the first time in this work, we manage to synthesize single-crystalline two-dimensional (2D) $SnNb_2O_6$ nanosheets with ultrathin structure through a facile one-step hydrothermal method. Comparative studies were explored to analyze the structure and phase evolution during the preparation course. The synthesized 2D structure demonstrated a narrower band gap of 2.09 eV and specific surface area of 76.1 $m^2\ g^{-1}$, which exhibited significantly extended visible-light-responsive range and larger surface area by contrast with the state-of-the-art reports, resulting in excellent visible-light-driven photoactivity towards H_2 production and water purification as well. Additionally, further enhanced photocatalytic performance was achieved by the incorporation of Pt as co-catalyst to indirectly indicate the advantage of the $SnNb_2O_6$ nanosheets in this method over other reported counterparts. It was found that, a very small amount of Pt loaded on the surface of $SnNb_2O_6$ nanosheets would contribute to remarkably higher activity than pure $SnNb_2O_6$ nanosheets and exhibit superior stability as well. Moreover, a deep insight into the underlying photocatalytic mechanism was proposed. This work sheds light on a new facile way to fabricate high-performance photocatalytic materials and provided new opportunities for solar-energy conversion.

Supplementary material for this article is available online

Keywords: one-step hydrothermal method, single crystal, $SnNb_2O_6$ nanosheets, photocatalytic reaction, mechanism

(Some figures may appear in colour only in the online journal)

* Authors to whom any correspondence should be addressed.

1. Introduction

Recently, semiconductor photocatalysis, one of the most promising approaches to achieve the conversion of solar energy into chemical energy [1–4], has gained considerable attention due to the depletion of global energy and steadily increasing environmental crisis [5, 6]. The development of advanced photocatalysts with superior performance and long cycle stability is still urgently needed [7–9]. Among all of the promising photocatalysts, niobates exhibit extremely potential due to their unique layer structure, physicochemical properties and excellent stability [10–14]. Up to now, some of niobates, such as $NaNbO_3$ [15], $SrNb_2O_6$ [16], $CaNb_2O_6$ [17] and $Ba_5Nb_4O_{15}$ [18], have been utilized in photocatalytic fields and demonstrated excellent performance. However, the photocatalytic efficiency is still limited owing to their wide band-gap of 3.0–4.7 eV, which means they can only be excited by ultraviolet (UV) or near-ultraviolet light [19, 20]. Nevertheless, the UV light just contributes 4% of the solar energy spectrum, while visible light accounting for almost 46%. Therefore, extending the light-responsive range of niobates to visible-light is a rational alternative to scale up its photocatalytic performance.

Additionally, the photocatalytic efficiency of a visible-light photocatalyst greatly depended on its optical absorption and efficient charge separation [21], which is closely related to their crystal structure, particle size and morphology [22–29]. Notably, two dimensional (2D) nanostructure captures much attention, as photocatalytic performance greatly benefits from its atomic-layer thickness and 2D anisotropy, which can produce more active sites and also reduce the recombination of electron–hole pairs [30–32]. As one typical niobate, $SnNb_2O_6$ has caught tremendous attention because of its 2D morphology and visible-light-responsive properties [33, 34]. Generally, $SnNb_2O_6$ contains a network of two-octahedron-thick sheet with corner-shared units of [NbO_6] and edge-shared [SnO_8] square antiprisms [35]. In comparison with other niobates, the distinct particularity of $SnNb_2O_6$ lies in its unique valence band, which consists of Sn5s and O2p orbitals. This uniqueness could significantly decrease its band gap and achieve more negative valence band position than that of other niobates [36, 37]. Therefore, the narrowing band gap of $SnNb_2O_6$ makes it possible for visible light harvesting.

However, the conventional preparation of $SnNb_2O_6$ always involves complex and laborious steps, which unavoidably introduces electronic defect into the host lattice and increases the reaction period and costs [38, 39]. For example, Chao *et al* synthesized $SnNb_2O_6$ nanosheets by multi-step hydrothermal reaction, during which $K_4Nb_6O_{17}$ nanosheets precursors were prepared first and then it was used to synthesize target products [40, 41]. Liang *et al* synthesized $SnNb_2O_6$ nanosheets using $Nb_2O_5{\cdot}nH_2O$ precursors. However, highly corrosive hydrofluoric acid was involved to fabricate $Nb_2O_5{\cdot}nH_2O$ [42, 43]. Seo *et al* fabricated $SnNb_2O_6$ nanoplates through a facile template-free solvothermal route. Nevertheless, the samples were invariably irregular and rough, which significantly restricted the photocatalytic activity [44]. Consequently, exploring a novel, facile and surfactant-free strategy to synthesize 2D $SnNb_2O_6$ nanosheets is still urgent.

In this work, 2D single-crystalline $SnNb_2O_6$ nanosheets were successfully fabricated through a facile one-step hydrothermal treatment for the first time. Various preparation conditions, such as the hydrothermal reaction temperature, pH and the oxygen content, were tuned to control the structural and morphological evolution of $SnNb_2O_6$. The water splitting as well as degrading organic dyes were used as probe reaction to investigate the photocatalytic performance under visible light irradiation. On the other hand, further improved performance of $SnNb_2O_6$ was explored by addition of Pt as co-catalyst to indirectly indicate the advantage of the $SnNb_2O_6$ nanosheets in this method over other reported counterparts. Additionally, a possible mechanism of $SnNb_2O_6$ systems in the photocatalytic process were discussed and proposed in detail.

2. Experimental

2.1. Preparation of $SnNb_2O_6$ nanosheets and Pt/$SnNb_2O_6$ nanosheets

2.1.1. $SnNb_2O_6$ nanosheets. The $SnNb_2O_6$ nanosheets were prepared by a one-step hydrothermal route. Typically, 1 mmol $SnCl_2$ (AR, Sinopharm Chemical Reagent Co. Ltd) and 2 mmol $NbCl_5$ (99.95%, Sinopharm Chemical Reagent Co. Ltd) were dissolved into 40 ml of deionized water and absolute ethanol, respectively. Afterwards, the latter was added dropwise to the former, followed by adjusting pH values to 2 via ammonium hydroxide (aq. 25%) under vigorous stirring. Then, the mixture was transferred to a 100 ml Teflon-lined autoclave and purged into nitrogen gas of 30 ml min^{-1} for 2 h to remove oxygen gas. Next, the mixture was heated at 200 and 230 °C for 48 h in an oven to yield yellow products. Finally, the yellow precipitates were filtered and washed with deionized water and absolute ethanol three or four times. On the other hand, the products synthesized at 230 °C without adjusting pH and purging with N_2 were also fabricated to make a contrast.

2.1.2. Pt/$SnNb_2O_6$ nanosheets. A series of Pt/$SnNb_2O_6$ nanosheets (the theoretical Pt loading in the products is 0.2 wt%, 0.5 wt%, 1.0 wt% and 2.0 wt%, respectively) were constructed by a simple *in situ* photo-reduction reaction. In detail, 0.2 g of the obtained $SnNb_2O_6$ nanosheets (230 °C) were dispersed in 40 ml of deionized water, and certain amount of aqueous $H_2PtCl_6{\cdot}6H_2O$ solution (10 mg ml^{-1}) was dropped. After stirring for 30 min, the above mixture was illuminated by 300 W Xe light at 25 °C for 4 h under magnetic stirring. Then, the product was centrifuged, washed

with deionized water three times and finally dried at 80 °C overnight in an oven.

2.2. Catalysts characterization

The details of characterization were offered in the supporting information.

2.3. Photocatalytic test

2.3.1. Photocatalytic hydrogen evolution. Water-splitting experiments were investigated in a top irradiation Pyrex flask equipped with a glass closed gas circulation system. Typically, 50 mg of the samples were suspended in 100 ml aqueous solution containing 20 vol% CH_3OH scavenger. Prior to irradiation, the above solutions were degassed several times to remove air under magnetic stirring and then irradiated with a 300 W Xe arc lamp (CeauLight, CEL-HXF300) connected with wavelength cut off filters for $\lambda \leqslant 420$ nm at 25 °C. The produced H_2 was measured by gas chromatograph with Ar as a carrier gas and a 5 A molecular sieve column.

2.3.2. The degradation of organic pollutant. The photocatalytic performance of the samples were also evaluated by the degradation of RhB aqueous solution ($10\ mg\ l^{-1}$) under visible light irradiation. In a typical procedure, 50 mg of the photocatalysts and 100 ml of RhB aqueous solution were added into a beaker at the temperature at 25 °C under magnetic stirring. The light source was a 300 W Xe arc lamp equipped with wavelength cut off filters for $\lambda \leqslant 420$ nm. After turning on the lamp, 5 ml of the suspension was fetched out at certain time intervals and centrifuged for UV–visible absorption spectrum measurements.

3. Results and discussion

3.1. Synthesis and characterization of photocatalysts

Generally, the reactant $SnCl_2$ is easily oxidized and its solubility changes with pH values of the solution [45, 46]. It is of great importance to control preparation parameters during the reaction process, such as the reaction temperature, pH values and dissolved oxygen. The morphology and microstructure of the samples obtained at different reaction conditions were firstly analyzed by SEM images and XRD patterns. As observed from the SEM images (figure 1(a)), the sample consists of large-scale congeries nanoparticles (NPS) and blocky shapes when the hydrothermal temperature was 200 °C along with purging with N_2 and pH of 2, and the corresponding XRD patterns are mainly attributed to SnO_2 (figure 2(Aa)). These results demonstrate $SnNb_2O_6$ nanosheets have not been formed at this temperature. Upon further extending temperature to 230 °C without adjusting pH, there are no noticeable changes in the shape and structure compared with that under 200 °C (figures 1(b) and 2(Ab)). In contrast, if maintaining the hydrothermal temperature at 230 °C without purging with nitrogen gas, the blocky shapes and NPS gradually decrease and quite a few nanosheets emerge on the surface of NPS (figure 1(c)). Meanwhile, new peaks could be observed from the corresponding XRD pattern, which are originated from the coexistent phase of SnO_2 and $SnNb_2O_6$ (figure 2(Ac)), suggesting $SnNb_2O_6$ starts to generate at the current condition. Nevertheless, because of the existence of dissolved oxygen, a small portion of Sn^{2+} in the solution is unavoidably oxidized, resulting in the presence of SnO_2 in the product. However, maintaining the temperature at 230 °C and purging with nitrogen gas under pH 2, dramatic changes of the morphologies can be seen. As observed from the SEM images (figure 1(d) and figure S1 is available online at stacks.iop.org/NANO/32/065705/mmedia), a large of 2D nanosheets with ultrathin thickness and lateral sizes of hundreds emerge at 230 °C. The corresponding XRD suggests the peaks belonging to SnO_2 were almost indiscernible. The main diffraction peaks located at 24.8°, 29.0°, 31.4°, 31.9°, 33.8°, 36.9°, 49.4°, 49.6°, 52.8°, 54.3°, 60.0°, 61.7° and 65.6° were assigned to the characteristic diffraction peaks of (−111), (311), (600), (002), (202), (020), (620), (022), (−113), (911), (−821), (331) and (−713) planes of $SnNb_2O_6$, which were consistent with the previously reported values of monoclinic $SnNb_2O_6$ (JCPDS card No. 84-1810) (figure 2(Ad)) [47]. These results indicated the $SnNb_2O_6$ nanosheets were successfully prepared at this reaction condition.

Furthermore, the structure of $SnNb_2O_6$ nanosheets was confirmed by FT-IR spectrum. As shown in figure 2(B), the absorption peaks considerably coincide with the state-of-the-art literatures [48]. And the peaks positioned at 670, 480 and $450\ cm^{-1}$ are assigned to the vibrations of the [NbO_6] octahedron including Nb–O bands, Nb–O–Nb bending, and lattice vibrations. The absorption bands at $1630\ cm^{-1}$ and $3400–3500\ cm^{-1}$ are ascribed to the stretching vibrations of O–H groups and hydrogen-bond [49], further demonstrating the successful preparation of $SnNb_2O_6$ nanosheets [50].

TEM and high resolution TEM (HRTEM) have been introduced to figure out the more detailed morphology of $SnNb_2O_6$ nanosheets. As shown in figures 3(a) and (b), the $SnNb_2O_6$ nanosheets present with comparatively thin thickness and smooth surface, which is consistent with the results of SEM. The thickness of $SnNb_2O_6$ nanosheets was measured by atomic force microscopy. As shown in figure S2, the observed thickness of the nanosheets is about 4 nm, which corresponds to 4–5 unit cells of $SnNb_2O_6$ [42]. The ultrathin structure makes it possible to have larger surface area and thus better photocatalytic performance. Besides, the distinct lattice spacing of $d = 0.300$, 0.280 and 0.310 nm match well with the (311), (002) and (−311) facets of $SnNb_2O_6$, respectively (figure 3(c)), again confirming the successful formation of $SnNb_2O_6$ nanosheets. The quite clear and orderly lattice fringes (taken from the region marked in figure 3(b)) show its superior crystallinity. It is well known that higher crystal quality can dramatically reduce the possibility of any grain boundaries and/or other interfaces (usually serve as recombination sites) of samples, which will facilitate the separation of photogenerated electron–hole pairs,

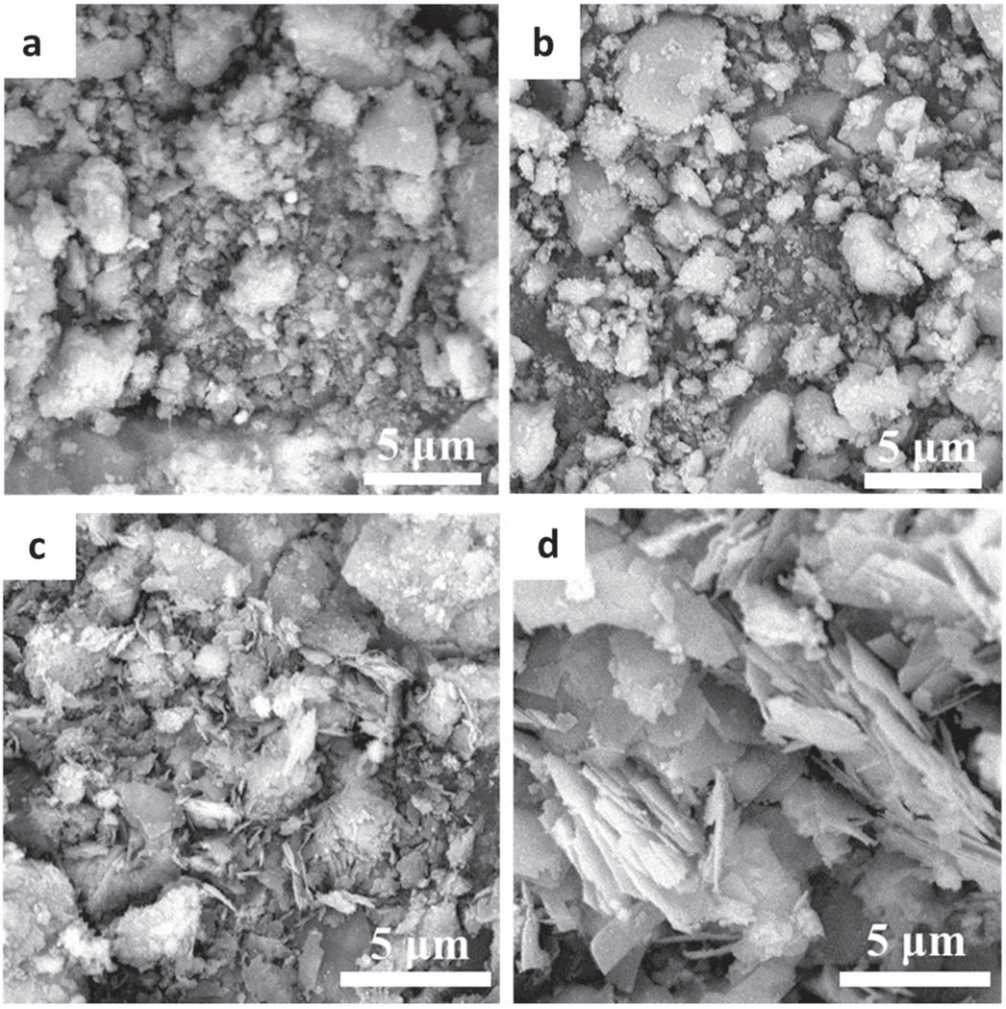

Figure 1. SEM images of niobates prepared at different reaction conditions: 200 °C along with purging with N_2 and adjusting pH with $NH_3{\cdot}H_2O$ (a), 230 °C prepared without adjusting pH with $NH_3{\cdot}H_2O$ (b), 230 °C prepared without purging with N_2 (c), 230 °C along with purging with N_2 and adjusting pH with $NH_3{\cdot}H_2O$ (d).

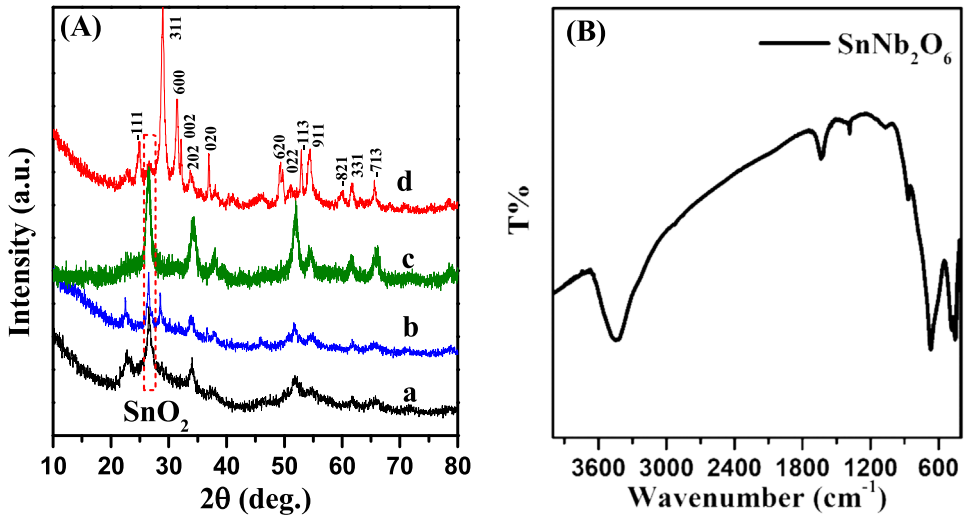

Figure 2. XRD patterns of niobate prepared at different reaction conditions (A): 200 °C along with purging with N_2 and adjusting pH with $NH_3{\cdot}H_2O$ (a), 230 °C prepared without adjusting pH with $NH_3{\cdot}H_2O$ (b), 230 °C prepared without purging with N_2 (c), 230 °C (d) and FTIR spectrum of $SnNb_2O_6$ nanosheets (B).

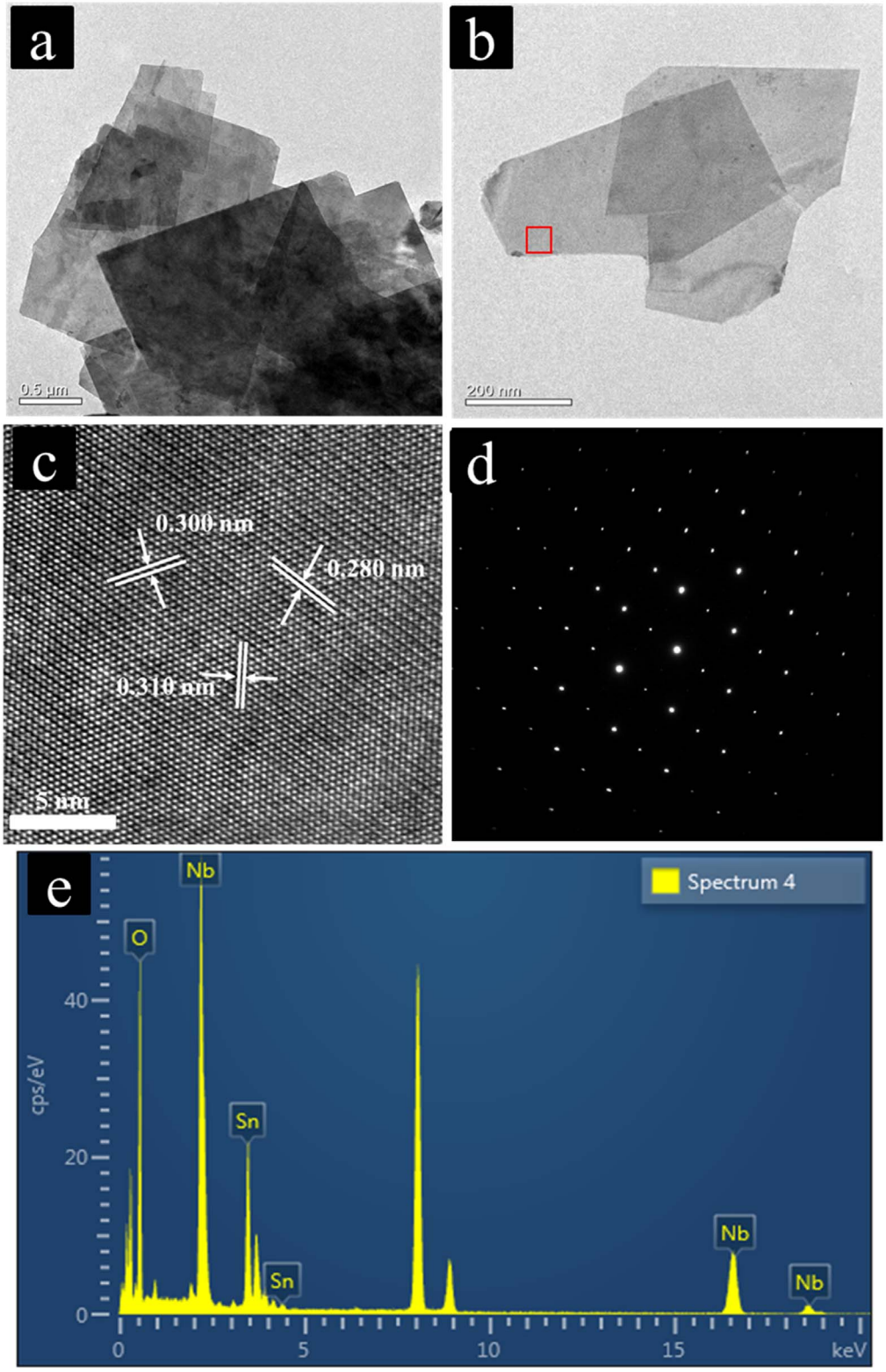

Figure 3. TEM and HRTEM images of $SnNb_2O_6$ (a)–(c) and the corresponding SAED (d) and EDS pattern (e) of $SnNb_2O_6$ nanosheets.

accordingly improving the photoactivity [51]. On the other hand, a typical selected area electron diffraction (SAED) pattern in figure 3(d) reveals that $SnNb_2O_6$ has a single-crystalline character. And only Sn, Nb and O elements in $SnNb_2O_6$ nanosheets can be detected (confirmed by energy dispersive x-ray spectroscopy (EDS) elemental scanning (figure 3(e))).

XPS analysis was carried out to investigate the chemical state of $SnNb_2O_6$ nanosheets. As shown in figure 4(a), the binding energies of 485.6 and 494.1 eV are attributed to Sn $3d_{5/2}$ and Sn $3d_{3/2}$, which indicated the chemical state of Sn

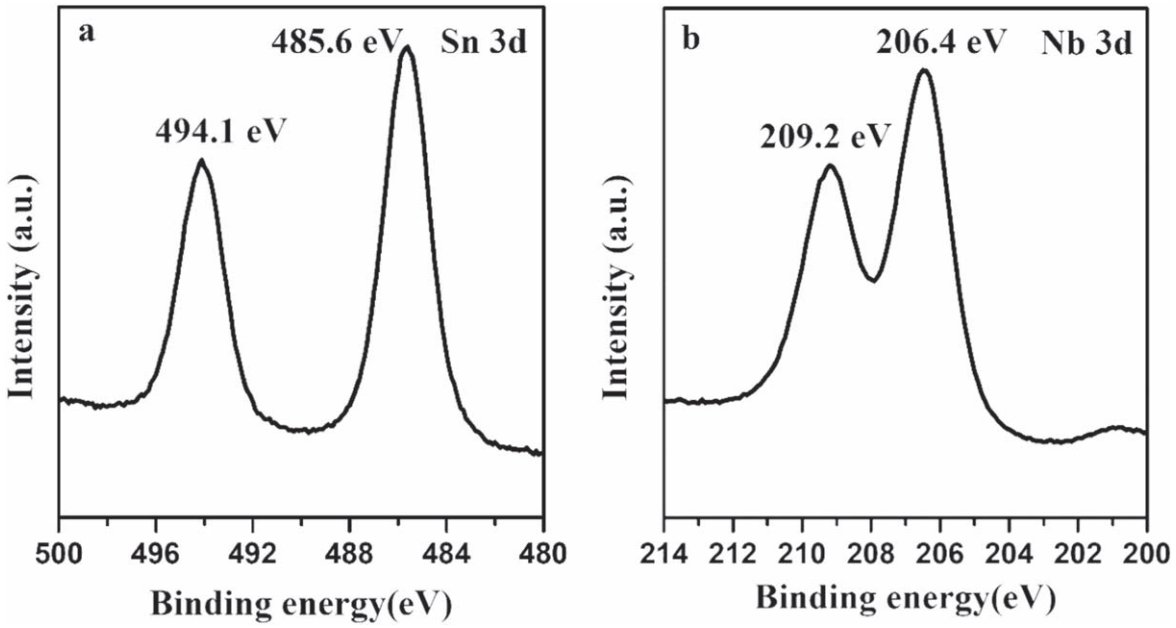

Figure 4. XPS survey spectra of $SnNb_2O_6$ in the Sn 3d (a) and Nb 3d (b) regions.

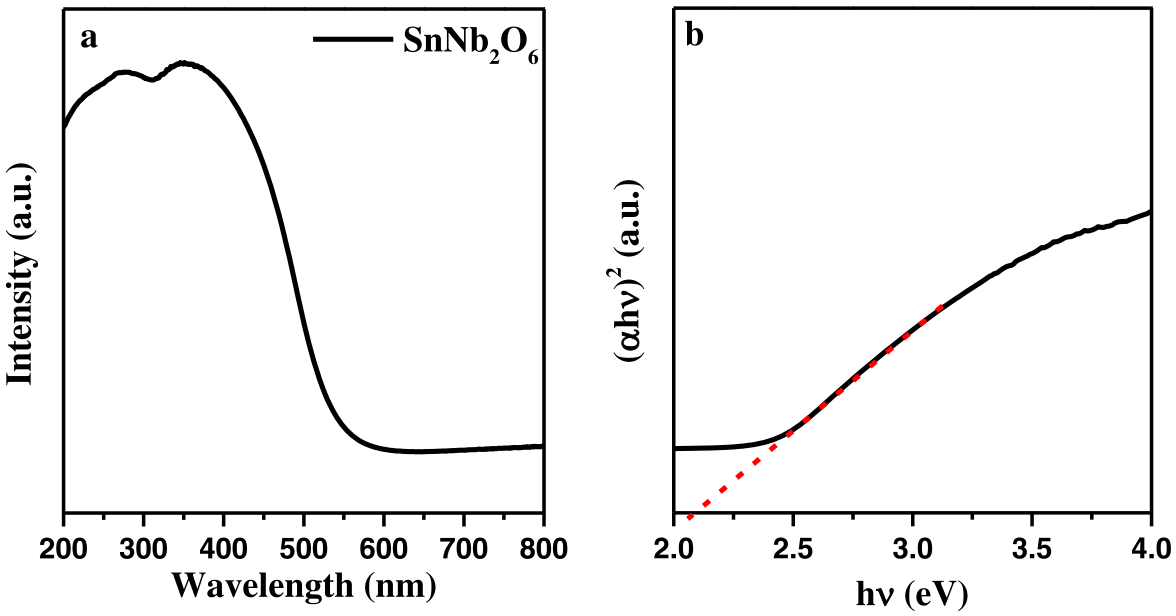

Figure 5. UV–Vis diffuse-reflectance spectra (a) and plots of $(ah\nu)^2$ versus $h\nu$ (b) of $SnNb_2O_6$.

element is Sn^{2+} [52], directly proving Sn^{2+} is not oxidized through one-step hydrothermal treatment. Simultaneously, the Nb 3d peaks of $SnNb_2O_6$ can be deconvoluted into two peaks located at 206.4 and 209.2 eV, demonstrating Nb is in the form of Nb (+5) chemical state (figure 4(b)).

3.2. Optical properties and BET analyses

Generally, the superior light absorption and higher surface area of a photocatalyst are intensely favored to its photocatalytic performance [53, 54]. Thus, the light absorption capability were firstly analyzed by UV–vis DRS. As shown in figure 5(a), $SnNb_2O_6$ nanosheets have an absorption edge at about 530–580 nm, suggesting the sample has strong absorption in the visible-light-responsive region. Also, the band gap energy of $SnNb_2O_6$ can be calculated by the Kubelka–Munk equation [55–57]:

$$ah\nu = A(h\nu - E_g)^{n/2}.$$

Here, a, E_g, ν and A are absorption coefficient, band gap energy, light frequency and a constant, respectively. And n represents the type of optical transition of a semiconductor ($n = 1$ for direct transition and $n = 4$ for indirect transition). Based on the previous report, the n value of $SnNb_2O_6$ is 1 [58]. Thus, according to the plot of $(ah\nu)^{2/n}$ versus $h\nu$, the E_g of $SnNb_2O_6$ is 2.09 eV (figure 5(b)). Table 1 shows the E_g comparison of $SnNb_2O_6$ in this work with the state-of-the-art reports. As can be seen, the E_g value of $SnNb_2O_6$ obtained by

Table 1. The band gap and surface area comparison of $SnNb_2O_6$ previously reported.

Synthesis method	E_g (eV)	S_{BET} ($m^2\ g^{-1}$)	References
Solid-state reaction	2.30	2.1	[43]
Multi-step hydrothermal reaction	2.59	22.8	[60]
Molten $SnCl_2$-treated	2.40	56.0	[61]
One-step hydrothermal treatment	2.09	76.1	This work

one-step hydrothermal treatment is obviously narrower than those of other methods. It is acknowledged that the relative narrowing band gap of a sample is greatly beneficial for extending its visible-light-responsive range [59], which will absorb more visible light to generate electron–hole pairs and in turn favor a photocatalytic reaction.

The specific BET surface area of $SnNb_2O_6$ nanosheets prepared by one-step hydrothermal treatment is 76.1 $m^2\ g^{-1}$ (table 1), presenting the largest surface area compared with other methods. Generally, photocatalysts with higher specific surface area is favorable to photocatalysis [62].

3.3. Photocatalytic tests

The photocatalytic performance of $SnNb_2O_6$ nanosheets was firstly evaluated through the photocatalytic hydrogen production under visible light irradiation. As shown in figure 6(a), the pure $SnNb_2O_6$ nanosheets exhibit H_2 evolution amount of 106.6 μmol g^{-1} after 4 h of reaction. Even without noble metal cocatalysts, the activity is still 2.8 times higher than $SnNb_2O_6$ prepared by solid-state reaction (table 2).

Additionally, as an effective way to improve the photocatalytic performance of semiconductor, $Pt/SnNb_2O_6$ nanosheets were constructed through *in situ* photo-reduction reaction to indicate the advantage of the $SnNb_2O_6$ nanosheets in this method over other reported counterparts. As illustrated in figure 6(a), the H_2 evolution amount could reach 239.8 μmol g^{-1} after 4 h, which is about 2.3 times greater than pure $SnNb_2O_6$ nanosheets. Moreover, the activity comparison of $SnNb_2O_6$ in this work with different preparation methods was displayed in table 2. As can be seen, although the photocatalytic performance changes with various factors, such as the mass of catalysts and irradiation wavelength, etc, a higher H_2 generation rate is still achieved under the similar reaction conditions by contrast with other preparation methods. Based on the results above, the optimal photocatalytic performance can be attributed to the following factors: (i) nanosheets with ultrathin 2D morphology and higher surface area can generate more active sites and have easier accessibility to the active sites; (ii) one-step hydrothermal method dramatically reduces the amount of defects, which facilitates the transformation of electrons; (iii) the narrowing band gap (confirmed by UV–vis DRS) extremely enhances its visible-light-harvesting capability.

The stability of $Pt/SnNb_2O_6$ nanosheets has been carried out as it is crucial to practical application. As demonstrated in figure 6(b), no distinct inactivation can be found after three repeated cycles, indicating $Pt/SnNb_2O_6$ nanosheets are sufficiently stable during the course of photocatalytic H_2 production.

On the other hand, the photocatalytic performance of pure $SnNb_2O_6$ nanosheets and the influence of Pt amount were also assessed through the photocatalytic aqueous-phase oxidation of RhB (a typical organic dyes) under visible light irradiation. As shown in figures S3 and S4, the concentration of RhB gradually degrades under visible light (about 50% after 360 min), while the self-photolysis of RhB without photocatalyst or visible light irradiation is almost negligible, indicating the sample possesses good photocatalytic activity towards the decomposition of pollutants. Besides, by contrast with pure $SnNb_2O_6$, all $Pt/SnNb_2O_6$ nanosheets show

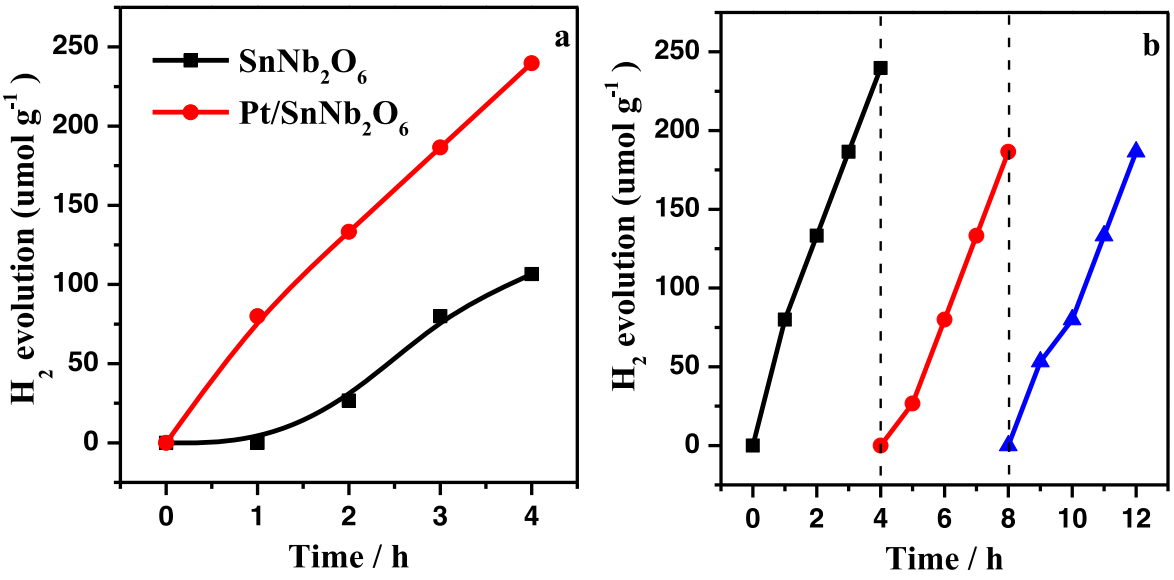

Figure 6. Photocatalytic H_2 generation (a) and recyclability (b) of various photocatalysts under visible light ($\lambda > 420$ nm) irradiation.

Table 2. Comparison of photocatalytic H_2 evolution activity over $SnNb_2O_6$ previously reported.

Synthesis method	Light source	Sacrificial agents	Cocatalyst	H_2 (μmol g^{-1} h^{-1})	References
Solid-state reaction	300 W Xe lamp ($\lambda > 420$ nm)	Methanol	1 wt% Pt	9.4	[43]
Multi-step hydrothermal reaction	300 W Xe lamp ($\lambda > 420$ nm)	Methanol	1 wt% Pt	59.9	[60]
Molten $SnCl_2$-treated	300 W Xe lamp ($\lambda > 420$ nm)	Methanol	0.3 wt% Pt	33.3	[61]
One-step hydrothermal treatment	300 W Xe lamp ($\lambda > 420$ nm)	Methanol	1 wt% Pt	60.0	This work

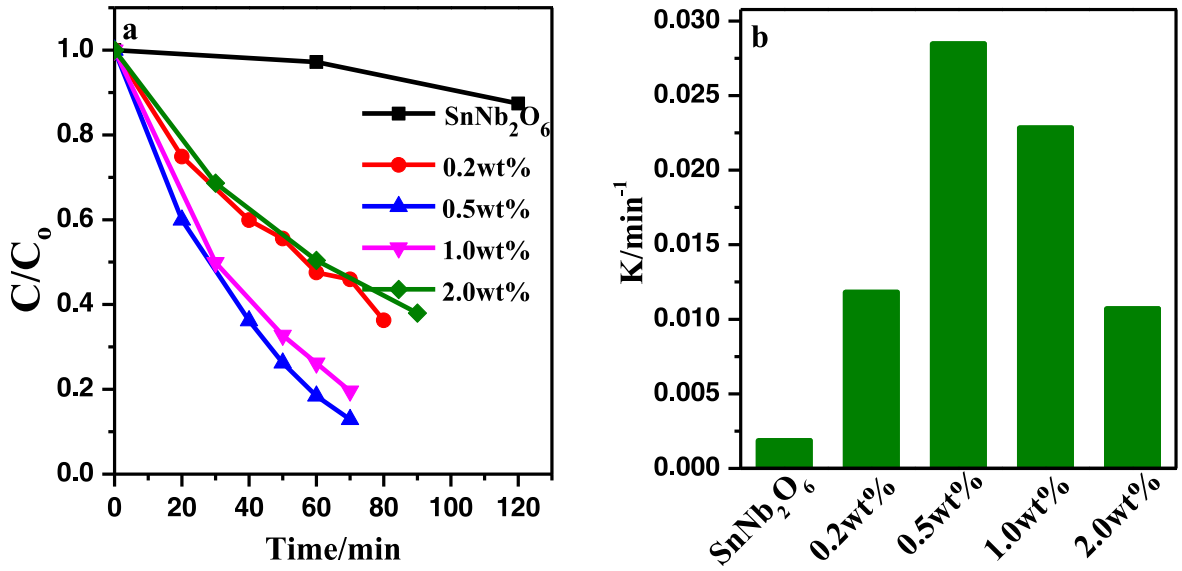

Figure 7. Photocatalytic degradation efficiency of RhB (a) and the apparent rate constants (b) of $Pt/SnNb_2O_6$ nanosheets under visible light ($\lambda > 420$ nm) irradiation.

appreciably much higher photocatalytic efficiency for the photo-degradation of RhB (figure 7(a)). Among which the $Pt/SnNb_2O_6$ nanosheets-0.5 wt% exhibits the most superior photocatalytic activity, approximately 100% of the RhB is eliminated from the solution in 70 min. The apparent first-order-rate constant (k) towards the degradation of RhB is calculated from a simplified Langmuir–Hinshelwood model and presented in figure 7(b) and table S1 [63]. It is clearly seen that the rate constant of $Pt/SnNb_2O_6$ nanosheets-0.5 wt% (0.029 min^{-1}) is greatly higher than those of pure $SnNb_2O_6$ nanosheets (0.002 min^{-1}), $Pt/SnNb_2O_6$ nanosheets-0.2 wt% (0.012 min^{-1}), $Pt/SnNb_2O_6$ nanosheets-1.0 wt% (0.023 min^{-1}) and $Pt/SnNb_2O_6$ nanosheets-2.0 wt% (0.011 min^{-1}). In addition, the rate constant of $Pt/SnNb_2O_6$ nanosheets-0.5 wt% is almost 15-fold higher than that of pure $SnNb_2O_6$ nanosheets, demonstrating very little Pt incorporation significantly increases the photocatalytic performance of $SnNb_2O_6$ nanosheets.

Besides, the recycling test for the degradation of RhB was performed to further confirm the synthesized material's stability. As illustrated in figure S5, the photocatalytic degradation efficiency of RhB is still approaching 90% even after 5 repeated runs, which indicates that $Pt/SnNb_2O_6$ nanosheets-0.5 wt% possesses sufficient stability for photocatalytic reactions.

3.4. The characterization and mechanism of $Pt/SnNb_2O_6$ nanosheets

To explore the reasons of photoactivity of $Pt/SnNb_2O_6$ nanosheets, we firstly investigated the morphology of the samples. The TEM images of $Pt/SnNb_2O_6$ nanosheets-0.5 wt% show a small amount of Pt NPS with a diameter of 1–2 nm is homogeneously dispersed on the surface of $SnNb_2O_6$ nanosheets (figure 8(a)), suggesting the interfacial interaction between Pt NPS and $SnNb_2O_6$ nanosheets. The corresponding EDS elemental scanning presents the existence of Pt, Sn, Nb and O elements (figure 8(c)), confirming the successful combination of Pt and $SnNb_2O_6$ nanosheets. However, further increment of Pt content to 2.0 wt% will result in the aggregation of Pt NPS, which limits the transfer of photo-induced charge carriers and further retard its photocatalytic performance (as demonstrated by the TEM image (figure 8(b))).

Moreover, FT-IR spectra were carried out to further reveal the structure of $Pt/SnNb_2O_6$ nanosheets. As shown in figure 9(a), all of the samples have similar profile with pure $SnNb_2O_6$, suggesting the structure is well maintained after incorporating with Pt NPS. However, the stretching model of Nb–O at 670 cm^{-1} shifts slightly to higher wavenumber along with the increment of Pt loading (figure 9(b)), which is possibly ascribed to the partial electron transfer between $SnNb_2O_6$ nanosheets and Pt NPS. This result indicates that interfacial interaction in the $Pt/SnNb_2O_6$ nanosheets exists,

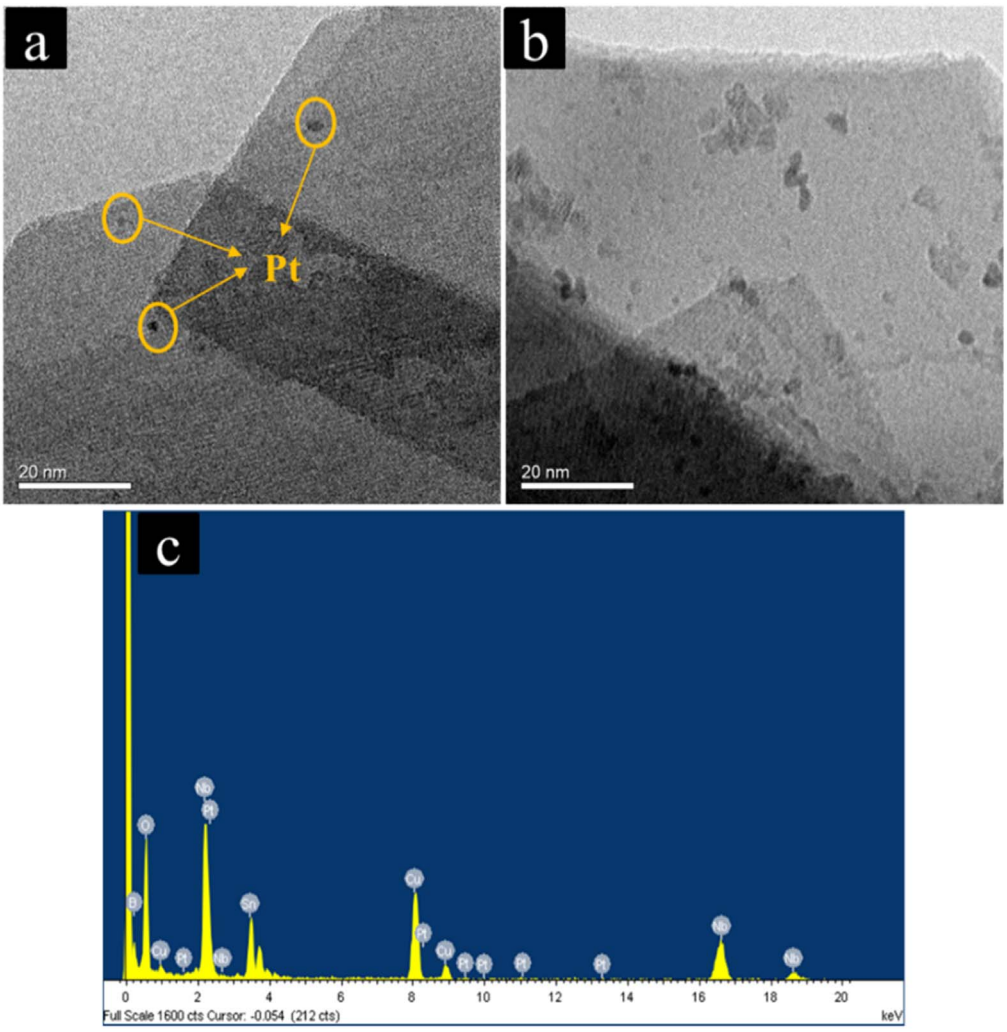

Figure 8. TEM images of $Pt/SnNb_2O_6$: 0.5 wt% $Pt/SnNb_2O_6$ (a), 2.0 wt%$Pt/SnNb_2O_6$ (b) and the EDS pattern of 0.5 wt% $Pt/SnNb_2O_6$ (c).

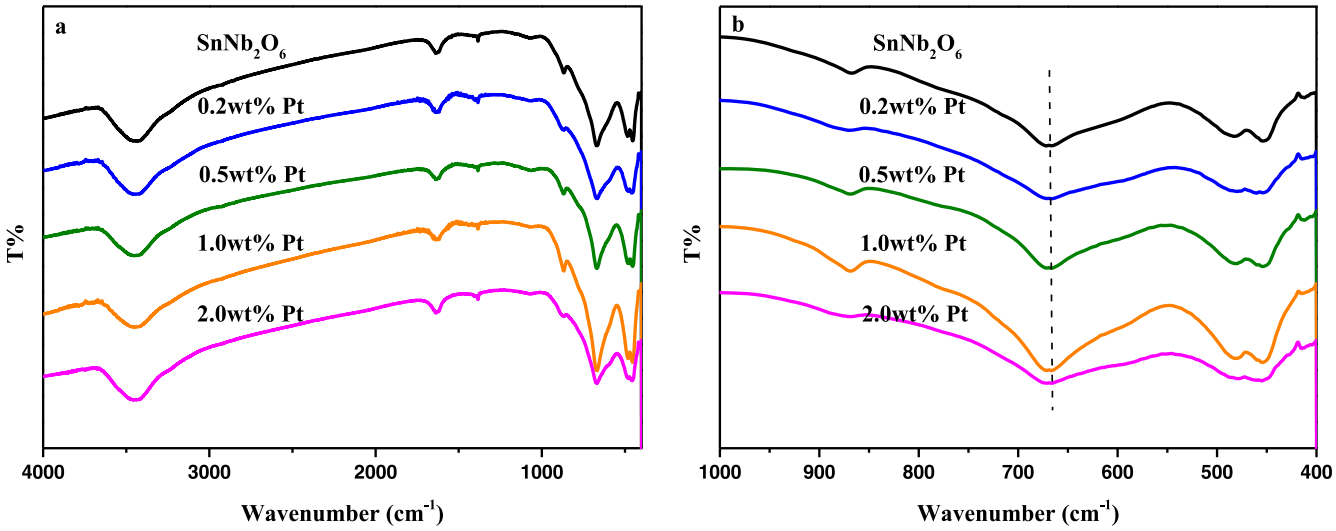

Figure 9. FT-IR spectra of the pure $SnNb_2O_6$ and $Pt/SnNb_2O_6$ (a), the magnified curves in the range of 400–1000 cm^{-1} (b).

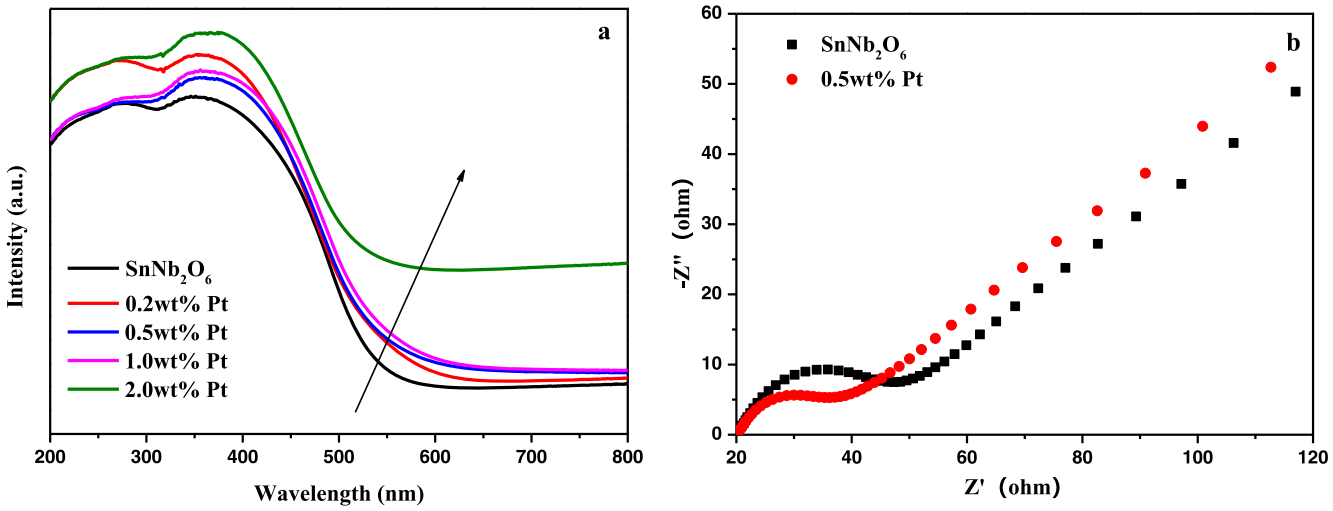

Figure 10. UV–Vis diffuse-reflectance spectra (a) and electrochemical impedance spectra (b) of $Pt/SnNb_2O_6$ nanosheets.

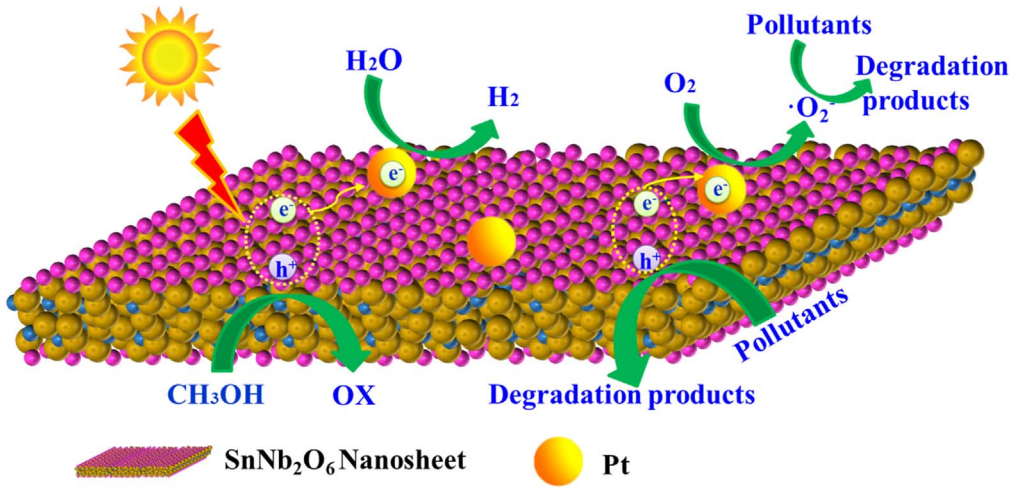

Scheme 1. Schematic illustration of the mechanism of $SnNb_2O_6$ nanosheet during the photocatalytic H_2 production and the photocatalytic degradation RhB under visible light irradiation.

which is well consistent with the results of TEM. It is well known that the metal-support interaction is greatly favorable for the separation of photoinduced electron–hole pairs, thus subsequently contributing to the enhancement of photoactivity [19].

The optical performance of $Pt/SnNb_2O_6$ nanosheets were analyzed by UV–vis DRS (figure 10(a)). It could be observed that the optical property obviously enhanced over the whole range with the increase of Pt amount. The significantly improved light harvesting are foreseeable to enhance their photocatalytic performance than pure $SnNb_2O_6$ nanosheets. Besides, EIS spectra was used to explore the separation efficiency of interfacial charge. As illustrated in figures 10(b) and S8, $Pt/SnNb_2O_6$ nanosheets demonstrate lower semicircle radius than that of pure $SnNb_2O_6$ nanosheets, confirming $Pt/SnNb_2O_6$ nanosheets have relative higher efficiency of charge separation.

Based on the results above, a possible photocatalytic reaction mechanism of the samples under visible light is illustrated in scheme 1. Due to the narrower band gap of $SnNb_2O_6$ nanosheets, more electron–hole pairs will be generated to participate in photocatalytic reaction under visible light irradiation. Subsequently, the electrons will be fast captured by the active sites exposed on the surface and reduce protons to hydrogen. Meanwhile, the holes react with methanol (sacrificial reagent) to retard the electron–hole recombination. After incorporating with Pt NPS, the photoinduced electrons will transfer to Pt NPS fast because of its highly dispersion and interfacial interaction, which significantly prolongs the lifetime of charge carriers. Subsequently, the electrons accumulated on Pt NPS could reduce protons to hydrogen. Besides, the electrons could be further trapped by molecular oxygen to yield $\cdot O_2^-$ radicals and utilize its powerful oxidizability to react with organic compounds [64]. On the other hand, the holes in the VB of $SnNb_2O_6$ nanosheet can also directly oxidize the organic compounds into CO_2, H_2O and so on. The introduction of Pt NPS not only results in a great enhancement of optical absorption, but also improves the separation efficiency of electron–hole pairs,

which will significantly increase the photocatalytic performance of $SnNb_2O_6$ nanosheets.

4. Conclusions

In summary, single-crystalline 2D $SnNb_2O_6$ nanosheets with ultrathin structure and larger surface area were successfully fabricated through one-step hydrothermal method for the first time. Experimental results show the morphology of $SnNb_2O_6$ was significantly determined by the hydrothermal reaction temperature, pH and the oxygen content. Besides, the photocatalytic activity confirmed $SnNb_2O_6$ nanosheets possessed super visible-light-driven photoactivity towards water purification and H_2 production due to the extended visible-light-responsive range, higher surface area and perfect 2D morphology. Additionally, a series of $Pt/SnNb_2O_6$ nanosheets prepared by *in situ* photodeposition suggested a very small amount of Pt doping would result in remarkably higher activity than pure $SnNb_2O_6$ nanosheets. Among which 0.5 wt% $Pt/SnNb_2O_6$ presented the best photocatalytic performance, appropriately 15 times higher than that of pure $SnNb_2O_6$ nanosheets. This work develops a new strategy for the development of novel photocatalytic materials with potential applications in solar energy conversion and environmental remediation.

Acknowledgments

This work was financially supported by the Natural Science Foundation of Shanghai [19ZR1403500], National Natural Science Foundation of China [22002102, 21373054, 21773291, 61904118], Natural Science Foundation of Jiangsu (BK20190935, BK20190947), Natural Science Foundation of the Jiangsu Higher Education Institutions of China [19KJA210005, 19KJB510012, 19KJB120005, 19KJB430034], Suzhou key laboratory for nanophotonic and nanoelectronic materials and its devices [SZS201812] and Jiangsu Key laboratory for environment functional materials.

Notes

The authors declare no conflict of interests.

ORCID iDs

Qianqian Liu https://orcid.org/0000-0003-0661-1139

References

[1] Tong H, Ouyang S X, Bi Y P, Umezawa N, Oshikiri M and Ye J H 2012 Nano-photocatalytic materials: possibilities and challenges *Adv. Mater.* **24** 229–51

[2] Wang H, Zhang L, Chen Z, Hu J, Li S, Wang Z and Wang X 2014 Semiconductor heterojunction photocatalysts: design, construction, and photocatalytic performances *Chem. Soc. Rev.* **43** 5234–44

[3] Cheng Q B and Yu J 2015 Graphene-based photocatalysts for solar-fuel generation *Angew. Chem. Int. Ed.* **54** 11350–66

[4] Wang X, Bi W, Zhai P, Wang X, Li H, Mailhot G and Dong W 2016 Adsorption and photocatalytic degradation of pharmaceuticals by $BiOCl_xI_y$ nanospheres in aqueous solution *Appl. Surf. Sci.* **360** 240–51

[5] Liang H, Tai X, Du Z and Yin Y 2020 Enhanced photocatalytic activity of ZnO sensitized by carbon quantum dots and application in phenol wastewater *Opt. Mater.* **100** 109674

[6] Lim P F, Leong K H, Sim L C, Aziz A A and Saravanan P 2019 Amalgamation of N-graphene quantum dots with nanocubic like TiO_2: an insight study of sunlight sensitive photocatalysis *Environ. Sci. Pollut. Res.* **26** 3455–64

[7] Low J, Jiang C, Cheng B, Wageh S, Al-Ghamdi A A and Yu J 2017 A review of direct Z-scheme photocatalysts *Small Methods* **1** 1700080

[8] Hak C H, Leong K H, Chin Y H, Saravanan P, Tan S T, Chong W C and Sim L C 2020 Water hyacinth derived carbon quantum dots and g-C_3N_4 composites for sunlight driven photodegradation of 2,4-dichlorophenol *SN Appl. Sci.* **2** 1–14

[9] Molaei M J 2019 A review on nanostructured carbon quantum dots and their applications in biotechnology, sensors, and chemiluminescence *Talanta* **196** 456–78

[10] Li G Q, Yang N, Wang W L and Zhang W F 2009 Synthesis, photophysical and photocatalytic properties of N-doped sodium niobate sensitized by carbon nitride *J. Phys. Chem.* C **113** 14829–33

[11] Cheng Z, Ozawa K, Osada M, Miyazaki A and Kimura H 2006 Low-temperature synthesis of $NaNbO_3$ nanopowders and their thin films from a novel carbon-free precursor *J. Am. Ceram. Soc.* **89** 1188–92

[12] Guo Y, Kakimoto K and Ohsato H 2004 Phase transitional behavior and piezoelectric properties of $(Na_{0.5}K_{0.5})NbO_3$-$LiNbO_3$$(Na_{0.5}K_{0.5})NbO_3$-$LiNbO_3$ ceramics *Appl. Phys. Lett.* **85** 4121–3

[13] Dutto F, Raillon C, Schenk K and Radenovic A 2011 Nonlinear optical response in single alkaline niobate nanowires *Nano Lett.* **11** 2517–21

[14] Kim S, Lee J H, Lee J, Kim S W, Kim M H, Park S, Chung H, Kim Y I and Kim W 2013 Synthesis of monoclinic potassium niobate nanowires that are stable at room temperature *J. Am. Chem. Soc.* **135** 6–9

[15] Lv J, Kako T, Li Z S, Zou Z G and Ye J H 2010 Synthesis and photocatalytic activities of $NaNbO_3$ rods modified by In_2O_3 nanoparticles *J. Phys. Chem.* C **114** 6157–62

[16] Chen D and Ye J H 2009 Selective-synthesis of high-performance single-crystalline $Sr_2Nb_2O_7$ nanoribbon and $SrNb_2O_6$ nanorod photocatalysts *Chem. Mater.* **21** 2327–33

[17] Cho I S, Kim D W, Cho C M, An J S, Roh H S and Hong K S 2010 Synthesis, characterization and photocatalytic properties of $CaNb_2O_6$ with ellipsoid-like plate morphology *Solid State Sci.* **12** 982–8

[18] Park S, Song H J, Lee C W, Hwang S W and Cho I S 2015 Enhanced photocatalytic activity of ultrathin $Ba_5Nb_4O_{15}$ two-dimensional nanosheets *ACS Appl. Mater. Interfaces* **7** 21860–7

[19] Liu Q Q, Zhang Q, Zhang L and Dai W L 2020 Highly efficient single-crystalline $NaNb_{1-X}Ta_XO_3$ ($X = 0.125$) wires: the synergistic effect of tantalum-doping and morphology on photocatalytic hydrogen evolution *J. Mater. Sci. Technol.* **54** 20–30

[20] Xu D, Yang S, Jin Y, Chen M, Fan W, Luo B and Shi W 2015 Ag-decorated $ATaO_3$ (A = K, Na) nanocube plasmonic

photocatalysts with enhanced photocatalytic water-splitting properties *Langmuir* **31** 9694–9

[21] Chai Y Y, Ding J, Wang L, Liu Q Q, Ren J and Dai W L 2015 Enormous enhancement in photocatalytic performance of Ag_3PO_4/HAp composite: a Z-scheme mechanism insight *Appl. Catal.* B **179** 29–36

[22] Liu Q, Zhang L, Chai Y and Dai W L 2017 Facile fabrication and mechanism of single-crystal sodium niobate photocatalyst: insight into the structure features influence on photocatalytic performance for H_2 evolution *J. Phys. Chem.* C **121** 25898–907

[23] Song S, Zhang Y, Xing Y, Wang C, Feng J, Shi W and Zhang H 2008 Rectangular AgIn $(WO_4)_2$ nanotubes: a promising photoelectric material *Adv. Funct. Mater.* **18** 2328–34

[24] Zhang L, Wang W, Zhou L and Xu H 2007 Bi_2WO_6 nano-and microstructures: shape control and associated visible-light-driven photocatalytic activities *Small* **3** 1618–25

[25] Yu J and Kudo A 2006 Effects of structural variation on the photocatalytic performance of hydrothermally synthesized $BiVO_4$ *Adv. Funct. Mater.* **16** 2163–9

[26] Joshi R K, Kanjilal A and Sehgal H K 2003 Size dependence of optical properties in solution-grown $Pb_{1-x}Fe_xS$ nanoparticle films *Nanotechnology* **14** 809–12

[27] Cho I S, Kim D W, Lee S, Kwak C H, Bae S T, Noh J H and Hong K S 2008 Synthesis of Cu_2PO_4OH hierarchical superstructures with photocatalytic activity in visible light *Adv. Funct. Mater.* **18** 2154–62

[28] Li R, Zhang F, Wang D, Yang J, Li M, Zhu J and Li C 2013 Spatial separation of photogenerated electrons and holes among {010} and {110} crystal facets of $BiVO_4$ *Nat. Commun.* **4** 1432

[29] Gao L and Zhang Q 2001 Effects of amorphous contents and particle size on the photocatalytic properties of TiO_2 nanoparticles *Scr. Mater.* **44** 1195–8

[30] Sun Y, Gao S, Lei F and Xie Y 2015 Atomically-thin two-dimensional sheets for understanding active sites in catalysis *Chem. Soc. Rev.* **44** 623–36

[31] Jiang D L, Wang T Y, Xu Q, Li D, Meng S C and Chen M 2017 Perovskite oxide ultrathin nanosheets/g-C_3N_4 2D-2D heterojunction photocatalysts with significantly enhanced photocatalytic activity towards the photodegradation of tetracycline *Appl. Catal.* B **201** 617–28

[32] Zhang J, Zhu Z P, Tang Y P, Müllen K and Feng X L 2014 Titania nanosheet-mediated construction of a two dimensional titania/cadmium sulfide heterostructure for high hydrogen evolution activity *Adv. Mater.* **26** 734–8

[33] Huang M, Liu J X, Huang P, Hu H and Lai C 2020 Self-assembly synthesis of $SnNb_2O_6$/amino-functionalized graphene nanocomposite as high-rate anode materials for sodium-ion batteries *Rare Met.* (https://doi.org/10.1007/s12598-020-01527-w)

[34] Cao J, Ma Y, Lv J, Ren S and Liu Y 2020 A potentiometric resolved photoelectrochemical system based on CdS nanowires and $SnNb_2O_6$ nanosheets: a case application for dual biomarker analysis *Chem. Commun.* **56** 1513–6

[35] Ren J, Ouyang S, Chen H, Umezawa N, Lu D, Wang D and Ye J 2015 Effective mineralization of organic dye under visible-light irradiation over electronic-structure-modulated $Sn(Nb_{1-x}Ta_x)_2O_6$ solid solutions *Appl. Catal.* B **168** 243–9

[36] Velikokhatnyi O and Kumta P 2010 *Ab initio* study of doped tin niobates and tantalates as prospective catalyst supports for water electrolysis *ECS Trans.* **28** 37–48

[37] Hosogi Y, Kato H and Kudo A 2008 Photocatalytic activities of layered titanates and niobates ion-exchanged with Sn^{2+} under visible light irradiation *J. Phys. Chem.* C **112** 17678–82

[38] Chen J, Yang H B, Miao J, Wang H Y and Liu B 2014 Thermodynamically driven one-dimensional evolution of anatase TiO_2 nanorods: one-step hydrothermal synthesis for emerging intrinsic superiority of dimensionality *J. Am. Chem. Soc.* **136** 15310–8

[39] Xun S, Zhang Z, Wang T, Jiang D and Li H 2016 Synthesis of novel metal nanoparitcles/$SnNb_2O_6$ nanosheets plasmonic nanocomposite photocatalysts with enhanced visible-light photocatalytic activity and mechanism insight *J. Alloys Compd.* **685** 647–55

[40] Zhou C, Chen G and Wang Q 2011 High photocatalytic activity of porous $K_4Nb_6O_{17}$ microsphere with large surface area prepared by homogeneous precipitation using urea *J. Mol. Catal.* A **339** 37–42

[41] Zhou C, Zhao Y, Shang L, Shi R, Wu L Z, Tung C H and Zhang T 2016 Facile synthesis of ultrathin $SnNb_2O_6$ nanosheets towards improved visible-light photocatalytic H_2-production activity *Chem. Commun.* **52** 8239–42

[42] Liang S, Liang R, Wen L, Yuan R, Wu L and Fu X 2012 Molecular recognitive photocatalytic degradation of various cationic pollutants by the selective adsorption on visible light-driven $SnNb_2O_6$ nanosheet photocatalyst *Appl. Catal.* B **125** 103–10

[43] Liang S, Zhu S, Chen Y, Wu W, Wang X and Wu L 2012 Rapid template-free synthesis and photocatalytic performance of visible light-activated $SnNb_2O_6$ nanosheets *J. Mater. Chem.* **22** 2670–8

[44] Seo S W, Noh T H, Park S, Lee C W, Kim S H, Kim H J and Hong K S 2014 Solvothermal synthesis of $SnNb_2O_6$ nanoplates and enhanced photocatalytic H_2 evolution under visible light *Int. J. Hydrog. Energy* **39** 17517–23

[45] Charbonnier M, Romand M, Harry E and Alami M 2001 Surface plasma functionalization of polycarbonate: application to electroless nickel and copper plating *J. Appl. Electrochem.* **31** 57–63

[46] Zhang Y C, Du Z N, Li S Y and Zhang M 2010 Novel synthesis and high visible light photocatalytic activity of SnS_2 nanoflakes from $SnCl_2 \cdot 2H_2O$ and S powders *Appl. Catal.* B **95** 153–9

[47] Hu T P, Dai K, Zhang J F and Chen S F 2020 Noble-metal-free Ni_2P modified step-scheme $SnNb_2O_6$/CdS diethylenetriamine for photocatalytic hydrogen production under broadband light irradiation *Appl. Catal.* B **269** 118844

[48] Lavat A E and Baran E J 2003 IR-spectroscopic characterization of $A_2BB'O_6$ perovskites *Vib. Spectrosc.* **32** 167–74

[49] Li Y L, Bian Y Y, Qin H X, Zhang Y X and Bian Z F 2017 Photocatalytic reduction behavior of hexavalent chromium on hydroxyl modified titanium dioxide *Appl. Catal.* B **206** 293–9

[50] Zhang Z, Jiang D, Li D, He M and Chen M 2016 Construction of $SnNb_2O_6$ nanosheet/g-C_3N_4 nanosheet two-dimensional heterostructures with improved photocatalytic activity: synergistic effect and mechanism insight *Appl. Catal.* B **183** 113–23

[51] Zhu S, Liang S, Bi J, Liu M, Zhou L, Wu L and Wang X 2016 Photocatalytic reduction of CO_2 with H_2O to CH_4 over ultrathin $SnNb_2O_6$ 2D nanosheets under visible light irradiation *Green Chem.* **18** 1355–63

[52] Li Q, Kako T and Ye J 2011 Facile ion-exchanged synthesis of Sn^{2+} incorporated potassium titanate nanoribbons and their visible-light-responded photocatalytic activity *Int. J. Hydrog. Energy* **36** 4716–23

[53] Wang S, Wang Y, Li L, Li L, Fu G, Shi R, Zou X, Zhang Z and Luo F 2020 Green synthesis of Ag/TiO_2 composites coated porous vanadophosphates with enhanced visible-light photodegradation and catalytic reduction performance for removing organic dyes *Dalton Trans.* **49** 7920-31

[54] Yang F, Zhang Q, Zhang L, Cao M, Liu Q and Dai W L 2019 Facile synthesis of highly efficient Pt/N-rGO/N-$NaNbO_3$

nanorods toward photocatalytic hydrogen production *Appl. Catal.* B **257** 117901

[55] Butler M A 1977 Photoelectrolysis and physical properties of the semiconducting electrode WO_2 *J. Appl. Phys.* **48** 1914–20

[56] Zeng J, Wang H, Zhang Y, Zhu M K and Yan H 2007 Hydrothermal synthesis and photocatalytic properties of pyrochlore $La_2Sn_2O_7$ nanocubes *J. Phys. Chem.* C **111** 11879–87

[57] Liu Q, Ding J, Chai Y, Zhao J, Cheng S, Zong B and Dai W L 2015 Unprecedented enhancement in visible-light-driven photoactivity of modified graphitic C_3N_4 by coupling with H_2WO_4 *J. Environ. Chem. Eng.* **3** 1072–80

[58] Ma X, Ma W, Jiang D, Li D, Meng S and Chen M 2017 Construction of novel $WO_3/SnNb_2O_6$ hybrid nanosheet heterojunctions as efficient Z-scheme photocatalysts for pollutant degradation *J. Colloid Interface Sci.* **506** 93–101

[59] Yu X, He J, Zhang Y, Hu J, Chen F, Wang Y, He G, Liu J and He Q 2019 Effective photodegradation of tetracycline by narrow-energy band gap photocatalysts $La_{2-x}Sr_xNiMnO_6$ ($x = 0$, 0.05, 0.10, and 0.125) *J. Alloys Compd.* **806** 451–63

[60] Jin Y, Jiang D, Li D, Xiao P, Ma X and Chen M 2017 $SrTiO_3$ nanoparticle/$SnNb_2O_6$ nanosheet 0D/2D heterojunctions with enhanced interfacial charge separation and photocatalytic hydrogen evolution activity *ACS Sustain. Chem. Eng.* **5** 9749–57

[61] Hosogi Y, Kato H and Kudo A 2006 Synthesis of $SnNb_2O_6$ nanoplates and their photocatalytic properties *Chem. Lett.* **35** 578–9

[62] Yang F, Ren J, Liu Q, Zhang L and Dai W L 2019 Facile oxalic acid-assisted construction of laminated porous N-deficient graphitic carbon nitride: highly efficient visible-light-driven hydrogen evolution photocatalyst *J. Energy Chem.* **33** 1–8

[63] Bian Z, Tachikawa T and Majima T 2012 Superstructure of TiO_2 crystalline nanoparticles yields effective conduction pathways for photogenerated charges *J. Phys. Chem. Lett.* **3** 1422–7

[64] Sharma S, Dutta V, Singh P, Raizada P, Rahmani-Sani A, Hosseini-Bandegharaei A and Thakur V K 2019 Carbon quantum dot supported semiconductor photocatalysts for efficient degradation of organic pollutants in water: a review *J. Clean. Prod.* **228** 755–69